MOX-Report No. 101/2023

Hybrid dimensional models for blood flow and mass transport

Formaggia, L.; Zunino, P.

MOX, Dipartimento di Matematica
Politecnico di Milano, Via Bonardi 9 - 20133 Milano (Italy)

mox-dmat@polimi.it https://mox.polimi.it

Chapter 17

Hybrid dimensional models for blood flow and mass transport

Luca Formaggia and Paolo Zunino
MOX, Department of Mathematics, Politecnico di Milano

ABSTRACT
Mathematical models accounting of several space scales have proved to be very effective tools in the description and simulation of the cardiovascular system. In this chapter, we review the family of models that are based on partial differential equations defined on domains with hybrid dimension. Referring to the vascular applications, the most prominent example consists of coupling three-dimensional (3D) with one-dimensional (1D) mathematical models for blood flow and mass transport. On the basis of their coupling conditions these models can be subdivided into two main categories: the ones based on sequential coupling and those arising from the embedded coupling. We organize this work in two main sections, reflecting this subdivision.

KEYWORDS
cardiovascular system, multiscale models, mixed-dimensional PDEs

17.1 INTRODUCTION

The human cardiovascular system is characterised by the presence of a wide variety of scales and characteristics: from the main blood vessels down to arterioles and capillaries. In addition to the complexities associated with the pulsatile nature of the flow and the difficulty to model the heart function, the flow behavior differs between the venous and arterial systems. Due to these complexities, the simulation of the local flow through the entire cardiovascular system is not only unfeasible, but also with little practical application. However, it is important to take a comprehensive approach, where the interactions of different parts of the system is accounted for by integrating models operating at different level of detail. It is the so-called (geometrical) multiscale (or hybrid-dimensional) modelling approach. One can envisage two types of hybrid dimensional models: sequential and embedded. In the first, pioneered in Formaggia et al. (1999), the aim is to maintain in a local detailed model the effect of systemic behaviour. A typical example is the coupling of a detailed three-dimensional model of blood flow in a

portion of artery with a simplified system made by a network of one-dimensional (or even compartmental (0D)) models of the rest of the cardiovascular system. In sequential hybrid dimensional models, the boundary conditions of the 3D model must be replaced by suitable interface conditions that allow the different model components to interact. The term "sequential" here indicates that the different models correspond to portions of the system that are physically adjacent each other, and the interaction is via conditions at the interface.

In an embedded multiscale model, components of different level of detail are superimposed on the same domain. A typical application is that of microcirculation. Here we have the presence of a complex vascular network formed by arterioles, capillaries and small veins immersed in the biological tissue.

Here the influence of the capillaries (which are highly interconnected) may be accounted for by changing the effective volumetric transport properties of the tissue, while the effects of larger vessels (which present a preferential direction of the flow) must be explicitly modeled. A possible technique is to couple a one dimensional model for the network of larger vessels with that governing mass flow and transport in the tissue. Compared to the previous serial hybrid models, where interface conditions are imposed at the boundary of the models, in the embedded models the exchange of mass is distributed along the curves that describe the vessels.

From the modeling standpoint, such ideas have appeared in the past three decades, (at least), for modeling wells in subsurface reservoirs in Peaceman (1978, 1983) and for modeling microcirculation in Blake and Gross (1982); Fleischman et al. (1986); Flieschman et al. (1986); Secomb et al. (2004). A similar approach has been recently used to model soil/root interactions Koch et al. (2018). However, these application-driven seminal ideas were not followed by a systematic theory and rigorous mathematical analysis. However, these models introduce additional mathematical complexity, in particular concerning the functional setting for the solution as it involves coupling PDEs on domains with high dimensionality gap. Such mathematical challenge has recently attracted the attention of many researchers. The sequence of works by D'Angelo (2007, 2012); D'Angelo and Quarteroni (2008), followed by Laurino, F. and Zunino, P. (2019); Köppl et al. (2018); Kuchta et al. (2021), have remedied the well-posedness by weakening the regularity assumptions that define a solution. An alternative approach is to decompose the solution into smooth and non-smooth components, where the non-smooth component may be represented in terms of Green's functions, and then consider the well-posedness of the smooth component, see Gjerde et al. (2019). Concerning approximability, elliptic equations with Dirac sources represent an effective prototype case that has been addressed in Bertoluzza et al. (2018); Köppl et al. (2016); Köppl and Wohlmuth (2014), where the optimal a-priori error estimates for the finite element approximation are derived. Furthermore, the interplay between the mathematical structure of the problem and solvers, as well as preconditioners for its discretization has been studied in details in Kuchta et al. (2016) for the solution of 1D differential

equations embedded in 2D, and more recently extended to the 3D-1D case in Kuchta et al. (2019).

In this work, we revise the sequential and embedded hybrid dimensional models for blood flow and mass transport, recalling the major results. In particular, the first part is dedicated to a review of different models for blood flow, with extensive references to the relevant literature.

17.1.1 Multiscale modeling of the cardiovascular system

In this Section we introduce the challenges of modeling blood flow in the cardiovascular system, from macro to micro, and prepare the reader to the main models to be addressed later. Blood is a complex fluid, in fact it is a suspension of particles, the most numerous being the erythrocytes, or red blood cells. The presence of suspended particles gives blood a non Newtonian behaviour, which means that the local stress is not proportional to the velocity gradients. Despite this, the incompressible Navier-Stokes equations are the most adopted model for the full three-dimensional simulation of blood flow in larger vessels. This is due to the difficulties of characterising the stress-strain relationships and the reduced relevance of non-Newtonian effects in larger vessels when the shear rate is usually above $100\, s^{-1}$ (see Kumar et al. (2017)). The equations should however be coupled with a model for the behaviour of the vessel walls, particularly if we want to account of the effect of pulse waves. The periodic variation in blood pressure, the associated pulsatile flow and all the effects of the transport through the vascular system are all induced by the compliance of the vessels.

The Navier-Stokes equations coupled with a simplified model of the vascular wall is also at the basis of the reduce one-dimensional model for blood flow in large vessels, whose derivation is outlined in Section 17.2. The starting point is a coupled fluid-structure problem that describes the evolution of the blood velocity $\boldsymbol{u}$ and pressure p, as well as the displacement $\boldsymbol{\eta}$ in the vessel wall. The fluid domain $\Omega_f(t)$ is changing with time because of the vessel compliance, therefore its configuration at each time t is determined by the position of its boundary $\partial\Omega_f(t)$ and can be obtained by defining a regular and invertible map from a reference domain $\hat{\Omega}_f$, denoted by $\mathcal{A}_t$ and called Arbitrary Lagrangian Eulerian (ALE) map:

$$\mathcal{A}_t : \hat{\Omega}_f \rightarrow \Omega_f(t); \quad \partial\Omega_f(t) \text{ given.} \tag{17.1}$$

The boundary $\partial\Omega_f(t)$ is composed by the interface with the vessel wall $\partial\Omega_f^s(t)$, whose configuration is determined by the vessel wall displacements, and the proximal and distal boundaries Γ_{in} and Γ_{out}. In this formulation a special role is played by the *domain velocity* $\boldsymbol{w} = \partial\mathcal{A}_t/\partial t$. More details may be found in Chapter 3 of Formaggia et al. (2010a).

Finally, the Navier-Stokes equations in the ALE frame may be written as

$$\begin{cases} \rho_f \dfrac{\partial \boldsymbol{u}}{\partial t} + \rho_f (\boldsymbol{u} - \boldsymbol{w}) \cdot \nabla \boldsymbol{u} - \mathbf{div}\boldsymbol{\sigma}_f (\boldsymbol{u}, p) = \mathbf{0} & \text{in } \Omega_f (t), \\ \operatorname{div} \boldsymbol{u} = 0 & \text{in } \Omega_f (t). \end{cases} \tag{17.2}$$

Here, ρ_f is the fluid density and $\boldsymbol{\sigma}_f (\boldsymbol{u}, p)$ is the Cauchy stress tensor, which takes the form

$$\boldsymbol{\sigma}_f (\boldsymbol{u}, p) = \mu_f (\nabla \boldsymbol{u} + \nabla^T \boldsymbol{u}) - p\boldsymbol{I}, \tag{17.3}$$

being μ_f and $\boldsymbol{I}$ the blood viscosity and the identity tensor, respectively.

Equations (17.2) are complemented by $\boldsymbol{u} = \partial \boldsymbol{\eta}/\partial t$ on $\partial \Omega_f^s (t)$ while boundary conditions at the proximal and distal sections, in a hybrid 3D-1D or 3D-0D model, will be determined by the coupling with the lower dimensional set of equations, as it will be detailed later on.

The movement of the domain is reflected in the equations by the appearance of a modified transport term, where the domain velocity $\boldsymbol{w}$ is subtracted from the fluid velocity. We also have to note that in (17.2) the time partial derivative is a derivative with respect the deforming frame, also called ALE time derivative. In the numerical setting this is quite handy. Indeed the domain will be typically partitioned in a computational grid that deforms in time to follow the changing domain and degrees of freedom are associated with grid nodes. The ALE derivative will then be the rate of change of nodal values.

In smaller vessels, compliance is often neglected. Additionally, at the velocity and length scales associated with these small vessel, the inertial effect appearing in the non-linear advective term in (17.2) is neglected, leading to the classic Stokes equations,

$$\begin{cases} \rho_f \dfrac{\partial \boldsymbol{u}}{\partial t} - \mathbf{div}\boldsymbol{\sigma}_f (\boldsymbol{u}, p) = \mathbf{0} & \text{in } \Omega_f, \\ \operatorname{div} \boldsymbol{u} = 0 & \text{in } \Omega_f. \end{cases} \tag{17.4}$$

As for the vessel wall deformation, two possible choice can be made. A full 3D elastic model could be adopted. It is customary in this case to write the equations in a reference domain, which is assumed to be stress-free and which we indicate as $\hat{\Omega}_s$, while $\boldsymbol{\eta} = \mathbf{x}(t) - \hat{\mathbf{x}}$ is the displacement of with respect to the reference configuration. This is indeed a classic Lagrangian representation, which gives rise to the following system of equations

$$\rho_s \frac{\partial^2 \boldsymbol{\eta}}{\partial t^2} - \mathbf{div}(\mathbf{F}\boldsymbol{\Sigma}) = \mathbf{0} \quad \text{in } \hat{\Omega}_s, \tag{17.5}$$

where $\mathbf{F} = \partial \boldsymbol{\eta}/\partial \hat{\mathbf{x}}$ is the *deformation gradient* and $\boldsymbol{\Sigma}$ the second Piola-Kirchoff tensor, which is a function of the *Green-Lagrange stress tensor* $\mathbf{E} = (\mathbf{F}^T \mathbf{F} - \boldsymbol{I})/2$. Details may be found in the cited reference. Equations (17.5) reduce to the classic equation of linear elasticity when the displacements may be considered

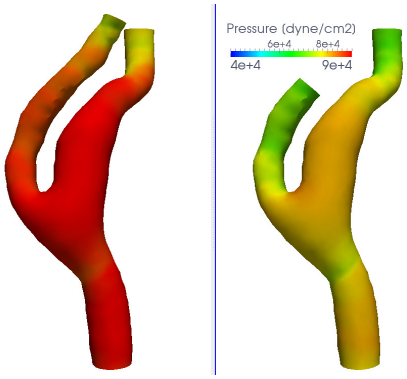

FIGURE 17.1 Pressure distribution in a model of a carotid artery computed with a full 3D model. The pictures show the pressure distribution at two different times.

as infinitesimal. In general, however, in the larger vessel we may consider the deformations small, but not the displacements, and a full non-linear formulation is required. The equation for the structure is coupled with the equation for the fluid though the boundary condition at the interface $\partial\hat{\Omega}_s^f$ between the two media, which expresses the continuity of the normal stresses,

$$\mathbf{F}\boldsymbol{\Sigma}\hat{\mathbf{n}} = J\boldsymbol{\sigma}_f(\boldsymbol{u}, p)\mathbf{F}^T\hat{\mathbf{n}}, \tag{17.6}$$

where $J = \det \mathbf{F}$.

Full scale three dimensional models has been used in several study of the haeamodynamics of large blood vessels, see Bennati et al. (2021); Crosetto et al. (2011); Savabi et al. (2020). In Figure 17.1 we show an example of the study of the blood flow in a real model of a carotid artery where a 3D fluid-structure model was adopted.

These type of 3D simulations are rather costly. The fact that the density of the wall tissue and that of blood are similar does not allow us to use some techniques often adopted in aerodynamics, where at each time step the fluid and structural problems are solved separately and only once. Those procedure will be unstable, due to the so called *added mass effect* analysed in Causin et al. (2005). Our class of problems requires instead to adopt more costly strongly coupled strategies, where at each time step the coupling conditions are satisfied exactly (or at least below a small tolerance). Therefore, when one is not interested in the stress distribution inside the vessel wall, but just to accounting for the effect of compliance, reduced structural models are adopted. A possibility is to use a *shell model*, see Chapter 3 of Formaggia et al. (2010a).

However, to simplify things further and have a less computationally demanding simulation, often one adopts a simple one dimensional model for the vessel displacements based on the following assumptions:

A.1 The blood vessel has a circular shape and the deformations in the radial

direction can be described by an homothety. It means that the displacement may be described by a scalar η proportional to the square root of the vessel cross section area A, i.e.

$$\eta \propto (\sqrt{A} - \sqrt{A_0}), \tag{17.7}$$

where A_0 is a reference vessel section area. The scalar η is the component of the displacement in the radial direction. The cross section area A normally refers to the cross section of the blood filled space.

A.2 The contribution of the fluid stresses in (17.6) is mainly due to pressure, so we neglect the contributions coming from the velocity gradients.

Thanks to assumptions A.1-A-2 we can write, for a single vessel of length L and wall thickness h_s, an equation of the type:

$$h_s \rho_s \frac{\partial^2 \eta}{\partial t^2} + a\eta - b\frac{\partial^2 \eta}{\partial z^2} = p - p_0, \quad z \in (0, L), \tag{17.8}$$

where a and b are parameters and p_0 a reference pressure.

Often, to further simplify the problem, one makes the following additional assumptions:

A.3 Quasi static formulation. The inertial term $\partial^2\eta/\partial t^2$ in (17.8) is neglected. It means that the vessel wall responds instantaneously to the pressure.

A.4 The term $b\partial^2\eta/\partial z^2$, is also considered negligible.

Under those additional assumptions, by recalling (17.7), we obtain a relation of the form,

$$p = p_0 + \beta(\sqrt{\frac{A}{A_0}} - 1), \tag{17.9}$$

where β is an elastic parameter linked to vessel wall elastic properties and thickness. Equation (17.9) is in fact a member of a family of relations of the form

$$p = p_0 + \phi(A, A_0, \boldsymbol{\beta}). \tag{17.10}$$

An example of a two parameter family of models where $\boldsymbol{\beta} = (\beta_0, \beta_1)$ and

$$\phi(A, A_0, \boldsymbol{\beta}) = \beta_0 \left[\left(\frac{A}{A_0} \right)^{\beta_1} - 1 \right]$$

has been considered in Martin et al. (2005).

These type of relations linking blood pressure to vessel section area are also at the basis of a class of one-dimensional models for blood flow in arteries adopted in studies on pulse wave propagation, for instance in Alastruey et al. (2007, 2008); Reymond et al. (2011), and that will be outlined next.

17.2 3D-1D GEOMETRIC SEQUENTIAL MULTISCALE MODELS

The resolution of the cardiovascular system with a full model is not only impractical, but also useless. Typically, a clinician is interested in the phenomena happening in a specific vessel or systems of vessels. For instance, studies of atherosclerotic plaques formation may benefit from the study of the blood flow pattern in the carotid. It is then useful to resolve that vessel with a full model. Yet, one has to account also of the rest of the circulatory system. This can be done by devising suitable boundary conditions, or, by accounting of the remaining part of the system by a reduced model. We will first consider the 1D model for the flow in a single vessel, dealing then with the problem of describing a whole network of vessels. We will then outline the compartmental models.

17.2.1 1D models for larger deformable vessels

We present here a one-dimensional model for blood flow in compliant vessels. This model is suited for larger vessels, where non-linear effect and wall compliance is relevant. A model more suitable for smaller vessels, adopted in studies of micro-circulation, will be presented in Section 17.3.1.

Let's consider a single vessel, which we assume of length L and of cylindrical shape. We indicate, as before, with $A = A(x)$ the area of a vessel cross section at the axial coordinate x, and with $Q = Q(x) = A(x)u(x)$ the volume flux in that section. Here u is the average axial velocity in the cross section. By integrating the Navier-Stokes equations (17.2) in a generic cross section, assuming that the viscous effects are relevant only near the vessel wall, we can derive the following system of hyperbolic equations Formaggia et al. (2010a),

$$\begin{cases} \dfrac{\partial A}{\partial t} + \dfrac{\partial Q}{\partial z} = 0 \\ \dfrac{\partial Q}{\partial t} + \dfrac{\partial}{\partial x}(\alpha^2 \dfrac{Q^2}{A}) + \dfrac{A}{\rho_f}\dfrac{\partial p}{\partial x} + K_R \dfrac{Q}{A} = 0, \end{cases} \tag{17.11}$$

for $x \in (0, L)$ and $t > 0$. Here, α is a parameter that depends on the velocity profile chosen when deriving the model and is usually set equal to 1, while K_R is a friction coefficient, which accounts of the dissipation effects of friction at the vessel wall boundary layer. It is related to blood viscosity. The system is closed by a pressure-area relation of the type (17.10), and here we will mainly refer to (17.9).

The analysis of the system can be found, for instance, in Formaggia et al. (2010a, 2001); Toro and Siviglia (2013), we will recall here the main results, relevant for the coupling with other models. The system is hyperbolic, which means that we can identify two characteristic variables with associated velocities. In particular, if we indicate here with $u = Q/A$ the average velocity in the vessel

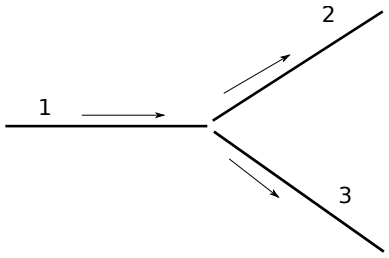

FIGURE 17.2 A sketch of a bifurcation.

cross section and with c the quantity

$$c = \frac{A}{\rho_f}\frac{\partial p}{\partial A},$$

the two characteristic velocities are given by $\lambda_{1,2} = u \pm c$, and the characteristic variable by $W_{1,2} = u \pm 4c$. System (17.11) can then be diagonalized, giving rise to

$$\begin{cases} \dfrac{\partial W_1}{\partial t} + \lambda_1 \dfrac{\partial W_1}{\partial x} = f(W_1, W_2), \\ \dfrac{\partial W_2}{\partial t} + \lambda_2 \dfrac{\partial W_2}{\partial x} = f(W_1, W_2), \end{cases}$$

where the forcing term f depends on the friction parameter and, possibly space variation of A_0 and β. For the typical values of blood flow velocity and vessels characteristics, we have $\lambda_1 > 0 > \lambda_2$, so the system describes the evolution of two waves travelling in opposite directions. This fact has implications in the choice of boundary conditions and the numerical treatment at the boundary, as detailed in Chapter 10 of Formaggia et al. (2010a) and discussed also in Formaggia et al. (2014).

17.2.2 Conditions at the boundaries and at the junctions

Indeed, at the boundary we are allowed to impose only information that affects the characteristic entering the domain, the value of the outgoing one being determined by the differential equations. An incorrect implementation of boundary conditions will induce *spurious waves* and degrade the solution. We refer to the cited references for more details. The existence of characteristics affects also the treatment at bifurcations. The model of a single vessel is in fact just one element for the construction of the 1D model of a vascular system. Let's consider the situation depicted in Figure 17.2 where vessel Ω_1 bifurcates into Ω_2 and Ω_3. We assume that the coordinate x local to each vessel domain is oriented for increasing values of x as in the Figure. We indicate with Q_i, A_i and p_i, for $i \in \{1, 2, 3\}$, the flux, area and pressure at the intersection for the corresponding vessel.

A stable set of conditions at the bifurcation implies *continuity of the total pressure* and *balance of mass*, see Formaggia et al. (2001). With the orientation of the vessels given in Figure, we have, at the intersection,

$$\begin{cases} Q_1 = Q_2 + Q_3, \\ p_1 + \frac{\rho_f}{2}\left(\frac{Q_1}{A_1}\right)^2 = p_2 + \frac{\rho_f}{2}\left(\frac{Q_2}{A_2}\right)^2, \\ p_1 + \frac{\rho_f}{2}\left(\frac{Q_1}{A_1}\right)^2 = p_3 + \frac{\rho_f}{2}\left(\frac{Q_3}{A_3}\right)^2. \end{cases} \tag{17.12}$$

These are three conditions that, due to the hyperbolic nature of the system, are sufficient to close the problem. However, at numerical level we need to complement them with three other conditions. They are derived from the fact that the outgoing characteristics are determined by the differential equations up to the boundary. If we indicate with λ_{ij} the i-th characteristic velocities of vessel j, and analogously for the characteristic variables W_{ij}, in our case the outgoing characteristics at the intersection are $W_{1,1}$, $W_{2,2}$ and $W_{2,3}$. Those three values must be determined by solving the corresponding differential equations up to the boundary. Numerically, there are different techniques for that purpose, like characteristic extrapolation or upwinding techniques. More details can be found in Chapter 10 of Formaggia et al. (2010a).

Once we have set up the interface condition, we can analyse pulse wave and average flow in a vascular network, like it has been done, for instance, in Alastruey et al. (2007, 2008); Blanco et al. (2015); Reymond et al. (2011). We only note that often relations (17.12) are simplified by considering pressure continuity instead of total pressure. Although this condition is not energy stable, it provides an an acceptable approximation and normally does not create stability problems at numerical level as the variation of $\rho_f (Q/A)^2$ are typically of order of magnitude smaller than that of pressure.

1D models are applicable only to larger vessels, therefore to close the circuit we need to represent distal circulation and the action of the heart. This can be done by resorting to compartmental models, also called lumped parameter models or 0D models.

17.2.3 Compartmental (0D) models

Compartmental models consider different parts of the vascular system as a "compartment" with an internal state composed typically by a pressure and a flow variable. They are often constructed with an analogy with electrical circuit. For instance, a possible compartmental model for flow in a vessel consider an averaged pressure $\tilde{P}$, and averaged flow $\tilde{Q}$ as state variable and the pressure and flow at the two ends, P_j and Q_j for $j = 1, 2$ as interface variables. It is given by

the following system of two ordinary differential equations

$$\begin{cases} C\dfrac{d\tilde{P}}{dt} + Q_2 - Q_1 = 0, \\ L\dfrac{d\tilde{Q}}{dt} + R\tilde{Q} + P_2 - P_1 = 0. \end{cases} \tag{17.13}$$

Here, C is the *compliance* that accounts for vessel elastic properties, L and inductance parameter related to blood inertia and R a resistance parameter that accounts for blood viscosity. The model for the different compartments are then connected using laws akin to Kirchhoff's electric circuit laws, which impose balance of fluxes and continuity of pressure. We should note that it is possible to derive different models for the same compartment, and the choice is sometimes made depending on the type of interface conditions that are desired. An analysis of lumped parameter models for the circulatory system is found in Milišić and Quarteroni (2004).

The 1D network model can then be completed by interfacing it with a compartmental model for the peripheral circulation and for the heart, as it has been done in Formaggia et al. (2006). The model for the heart is not detailed here for the sake of conciseness, but is also formed by a system of ordinary differential equations with the presence of an activation term that accounts for heath pumping action and a model for closure and aperture of the cardiac valves.

17.2.4 1D models for blood solutes

The 1D models can be extended also for the transport of blood solute. Indeed, once we have the flux field Q we may solve a transport-diffusion-reaction problem for the transport of solutes along the vascular network. In the simple case of a single solute and linear reaction term we have an equation for the concentration c of the type

$$\frac{\partial c}{\partial t} + \omega\frac{\partial^2 c}{\partial x^2} + u\frac{\partial c}{\partial x} + K_c c = 0,\ 0 < x < L, t > 0, \tag{17.14}$$

where ω and K_c are the diffusion and reaction parameter. At the intersections one imposes continuity of concentrations. More complex models will be presented in a later Section, when dealing with immersed multiscale setting.

A note is here necessary. We have omitted in the various models to indicate the initial conditions, which of course are required. The issue of initial conditions in the simulation of blood flow phenomena is problematic. The actual physical problem exhibit periodic solutions, corresponding to the heart beat. Therefore a common practice is to start with a arbitrary (but realistic) initial condition and let the simulation run for at least three heart beats, until the solution reaches a periodic regime.

17.2.5 Sequential coupling of 3D and 1D models

The coupling of a 3D model with a 1D model may help in representing correctly the pulse waves entering and exiting the 3D domain. However, some important observations have to be made, listed in the following, where with Γ we indicate the interface between the two models,

1. The 1D model governs the evolution of averaged quantities. The pressure in the 1D model is in fact the average pressure on the cross section, while $Q = Au$ is the product of the section area and the average velocity on the section. The standard boundary conditions for the Navier-Stokes problem require instead the availability of either velocity or normal stresses on each point of Γ. To overcome this problem, we need to formulate the interface conditions for the full dimensional model in terms of *defective boundary conditions*. One of the first attempts in this direction is illustrated in Veneziani and Vergara (2005) for the flow rate problem and rigid walls, i.e. for the imposition of an average velocity. The technique has then been extended to consider compliant vessels in Formaggia et al. (2010b). A review on defective boundary conditions is found in Formaggia and Vergara (2012).
2. We then have to address which quantities have to be transferred between the models. The idea investigated in Formaggia et al. (2012) is to devise a coupling that guarantees no spurious energy loss or creation at the interface Γ. It has been found that this can be accomplished by imposing on Γ the continuity of mass flux and averaged total pressure,

$$\begin{cases} \int_\Gamma \boldsymbol{u} \cdot \mathbf{n} = Q_{1D} \\ \int_\Gamma \sigma(\boldsymbol{u}, p_{tot})\mathbf{n} = -\left[p_{1D} + \dfrac{\rho_f}{2}\left(\dfrac{Q_{1D}}{A_{1D}}\right)^2 \right]\mathbf{n}, \end{cases} \tag{17.15}$$

   where the suffix $1D$ indicate the quantities in the 1D model, $p_{tot} = p + \frac{\rho_f}{2}|\boldsymbol{u}|^2$ and $\mathbf{n}$ is the normal to Γ. In the same reference energy preserving conditions for the vessel walls are also indicated.
3. A final aspect concerns how to implement the coupling numerically. A monolithic approach, where the full and reduced model are advanced together is effective, but also costly. One normally resorts to partitioned strategies, where the solution of the full 3D problem and that of the 1D network is carried out sequentially. This has also the advantage of enabling to use two existing codes for the 3D and 1D problems without the need of integrating them. However, it has been found that the partitioned scheme should be implicit, i.e. at each time step sub-iterations are needed between the 3D and 1D problems, until the interface conditions are met up to a prescribed tolerance. An analysis of partitioned schemes can be found in Malossi et al. (2013), while a derivation of the interface condition based on a variational formulation is available in Chapter 9 of Ambrosi et al. (2012).

17.3 3D-1D GEOMETRIC EMBEDDED MULTISCALE MODELS

In the second part of this work we address the coupling of a vascular network with the surrounding environment. This point of view is typically adopted at the level of microcirculation, for modeling the interaction of small vessels (arterioles, capillaries, venules) with a biological tissue. Thanks to the growing specialization of the models and of the numerical solvers, it is today possible to address direct simulations of the interaction of microcirculation with the biological environment at the level of functional portions of tissue. In Hartung et al. (2021), massive simulations over sizeable portions of mouse cortex (e.g. a cube of tissue 3 mm wide), have been performed, encompassing about 10^6 vascular segments. Similarly, Sweeney et al. (2019) have performed in-silico studies modelling the transport of fluid through orthotopic murine gliomas and human colorectal carcinoma xenograft grown subcutaneously in 8–10 week old, female mice. I this case as well, the whole microvasculature was reconstructed and simulated, involving about 10^5 vascular segments. Obviously, to achieve such a detailed description of the microvessels on fairly portions of tissue, a *brute force* approach, where the vessels are represented as 3D channels is not viable. On one hand it would require enormous efforts for the construction of a computational grid capturing all the geometrical details of the problems. On the other hand, the corresponding numerical simulation would exceed reasonable costs. The previous approaches, are in fact based on model reduction strategies, that in any case aim to simplify the modeling and computational burden of describing the microcirculation, yet providing a detailed geometrical representation of it. These strategies have been successfully applied to model and simulate the microcirculation in complex networks and the related transport phenomena in Cattaneo and Zunino (2014a,b); Nabil et al. (2015); Nabil and Zunino (2016); Possenti et al. (2019b,a, 2020); Cicchetti et al. (2020); Offeddu et al. (2019); Possenti et al. (2021), listed as representative examples of many other works.

The aim of this section is to develop a 3D-1D coupled model for the interaction of a biological tissue (t) with the blood vessels (v) embedded into it. Before describing the model, we point out some relevant difference between the systemic circulation and the peripheral circulation, i.e. microcirculation. First, because of the huge resistance that blood has to overcome to reach the peripheral districts, in the latter case the blood flow is not longer pulsatile. For this reason, it is acceptable to adopt a quasi-static modeling approach. In other words, the periodic deformation of the vascular cross section is negligible. Another difference with respect to the models addressed in previous section consists in the coupling, which in this case take place along the whole surface of the vascular network. Considering the high density of small vessels per unit volume, it makes the 3D-1D problem to be fully coupled.

We consider a domain Ω that is composed by two parts, Ω_v and Ω_t, the capillaries and the tissue, respectively. Assuming that the capillaries can be described as cylindrical vessels, we denote with Γ the outer surface of Ω_v, with

R its radius and with Λ the centerline of the vascular network. Any physical quantity of interest, such as the pressure p_v, p_t (where subscripts v, t stand for vascular and tissue respectively) and the velocity $\boldsymbol{u}_v$, $\boldsymbol{u}_t$, is a function of space (being $\boldsymbol{x} \in \Omega$ the spatial coordinates). We consider steady-state flow conditions, as a result all variables are independent of time.

The flow model in the vascular domain Ω_v reads as follows:

$$\begin{aligned} \rho \frac{\partial \boldsymbol{u}_v}{\partial t} + \rho(\boldsymbol{u}_v \cdot \nabla)\boldsymbol{u}_v = \nabla \cdot \boldsymbol{\sigma} \quad & \text{in } \Omega_v, \\ \nabla \cdot \boldsymbol{u}_v = 0, \quad & \text{in } \Omega_v, \end{aligned} \tag{17.16}$$

where $\boldsymbol{\sigma}(\boldsymbol{u}_v, p_v) = 1/2\mu_v(\nabla \boldsymbol{u}_v + \nabla^T \boldsymbol{u}_v) - \nabla p_v$ is the Cauchy stress in the blood and μ_v is the apparent (or effective) blood viscosity, accounting for non-Newtonian flow.

The behavior of the tissue can be modeled as an isotropic porous medium. As a consequence, the Darcy's law is used to describe the fluid permeation across the tissue, together with the mass balance equation for incompressible fluids. We denote by μ_t and K the dynamic fluid viscosity and the hydraulic permeability of the interstitial tissue, respectively, and ρ is the blood density. The viscosity of the interstitial fluid, μ_t, is taken from Swartz and Fleury (2007). It is comparable to the one of blood plasma at body temperature of $37^o C$.The lymphatic system drains the excess of fluid from the interstitial space to the venous system. Such drainage is taken into account by including a sink term, which is defined by the hydraulic conductivity of the lymphatic wall, denoted here by L_p^{LF}, the surface area of the lymphatic vessels per unit volume of tissue, $\frac{S}{V}$, and the hydrostatic pressure difference between the interstitial space and the lymphatic vessels, p_L. The flow model in the tissue consists of the following governing equations:

$$\begin{aligned} \boldsymbol{u}_t + \frac{\mathrm{K}}{\mu_t} \nabla p_t = 0, \quad & \text{in } \Omega_t, \\ \nabla \cdot \boldsymbol{u}_t + L_p^{LF} \frac{S}{V}(p_t - p_L) = 0, \quad & \text{in } \Omega_t, \\ \boldsymbol{u}_t \cdot \boldsymbol{n} = \beta_t(p_t - p_0), \quad & \text{on } \partial\Omega_t. \end{aligned} \tag{17.17}$$

At the interface $\Gamma = \partial\Omega_v \cap \partial\Omega_t$ we impose continuity of the flow:

$$\begin{aligned} \boldsymbol{u}_v \cdot \boldsymbol{n} = \boldsymbol{u}_t \cdot \boldsymbol{n} = f(p_t, p_v), \quad & \text{on } \Gamma \\ \boldsymbol{u}_t \cdot \boldsymbol{\tau}_k = 0, \quad & \text{on } \Gamma \\ f(p_t, p_v) = L_p\big((p_v - p_t) - (\pi_v - \pi_t)\big), & \end{aligned} \tag{17.18}$$

where $\boldsymbol{n}$ is the outward unit vector normal to the vascular surface and $\boldsymbol{\tau}_k$, $k = 1, 2$ are the tangential and binormal vectors. The fluid flux across the vascular wall can be obtained on the basis of linear non-equilibrium thermodynamic arguments. In particular L_p is the hydraulic conductivity of the vessel wall. In (17.18) π_v and π_t determine the osmotic (or oncotic) pressure gradient across

the vascular wall, namely $\delta\pi = \pi_v - \pi_t$, mainly due to the difference in the concentration of proteins (for example albumin), Landis and Pappenheimer (1963). In what follows, we assume that $\delta\pi$ is given and is independent of $\boldsymbol{x}$.

17.3.1 1D models for rigid vessels

To model blood flow through small blood vessels, we exploit assumptions about the steady nature of the flow and its low speed to derive a simplified version of the governing equations (17.16), addressed in the next subsection.

17.3.1.1 1D model for steady flow in a curved cylinder

The one dimensional model that governs the bulk flow in each branch of a generic microcirculation network is obtained as follows. Let us define a local cylindrical coordinate system $\boldsymbol{x} = (r, \theta, s)$ at each point of the centerline of the capillaries. We denote with $\boldsymbol{e}_r, \boldsymbol{e}_\theta, \boldsymbol{e}_s$ the radial, circumferential and axial unit vectors. The model is based on the following, geometric, kinematic and dynamic assumptions: **circular section** - for each value of the arc length s along a network branch, the intersection between the orthogonal plan to $\boldsymbol{e}_s$ and the vessel is circular; **dominance of axial velocity** - the radial and circumferential velocity components are negligible compared to the axial component, namely $\boldsymbol{u}_v = [0, 0, u_v(r, \theta, s)]^T$; **body forces** - we neglect the effect of gravity and other possible types of body forces (inertia, Coriolis); **steady flow** - we neglect transient phenomena, in fact microcirculation is characterized by negligible fluctuations of the blood pressure due to the heartbeat, namely the Womersley numbers at the level of microvascular circulation are negligible Guyton et al. (1971). For this reasons, we just aim to determine the steady flow conditions; **dominance of viscous forces** - microcirculation is also characterized by the dominance of viscous forces over inertial forces acting on infinitesimal fluid particles, namely the Reynolds number characterizing the flow is low; **viscosity** - we assume that the apparent viscosity of blood, μ_v is independent of the local deformation rate conditions. However, the viscosity is not a constant parameter but it depends on the hematocrit and on the vessel radius.

Under these assumptions the mass balance and momentum equations governing an incompressible flow, such as blood, reduce to the following form,

$$u_r = u_\theta = 0, \partial_r p_v = 0,\ \partial_\theta p_v = 0,\ \partial_s u_v = 0,\ -\mu_v \Delta u_v + \partial_s p = 0, \quad (17.19)$$

for any $(r, \theta, s) \in \Omega_v$ where Δ denotes the Laplace operator with respect to cylindrical coordinates $\Delta u = 1/r\partial_r(r\partial_r u) + 1/r^2\partial^2_\theta u + \partial^2_s u$. We now aim to transform equation (17.19) into a simpler one that is defined on the centerline of the channel. To this purpose, we assume that each branch is a generalized cylinder with circular cross section of radius R. We introduce a parametrization of each curvilinear branch. Let $\boldsymbol{\Psi} : \mathbb{R} \to \mathbb{R}^3$ be the parametric arc length, such that $\boldsymbol{\Psi} \in C^3(\mathbb{R})$ and $\|d_z \boldsymbol{\Psi}(z)\| = 1$ for any $z \in [0, L]$ being L the length of

a generic branch of the vascular network. Note that $s = \int_0^z \|d_\zeta \mathbf{\Psi}(\zeta)\| d\zeta = z$. The curvature of the arc at a specific location, is $\kappa = \|d_{ss}\mathbf{\Psi}(s)\|$; the centripetal unitary direction is $\boldsymbol{N} = d_{ss}\mathbf{\Psi}(s)/\kappa$ and the center C_0 of the osculating circle is the point in the direction $\boldsymbol{N}(s)$ with distance $1/\kappa$ from $\mathbf{\Psi}(s)$.

In order to proceed with the one-dimensional model derivation, we set the following ansatz: *the axial velocity profile can be decomposed as* $u_v(r,\theta,s) = \overline{u}_v(s)\Phi(r,\theta)$ *where* $\overline{u}_v$ *represents the mean or bulk velocity of the blood stream on the cross section identified by the arc length s, denoted by* $\Sigma(s)$. More precisely, in what follows we will use the notation

$$\overline{u}_v(s) = \frac{1}{\pi R^2}\int_{\Sigma(s)} \boldsymbol{u}_v \cdot \boldsymbol{n}\, d\Sigma\,,$$
$$\overline{p}_v(s) = \frac{1}{\pi R^2}\int_{\Sigma(s)} p_v\, d\Sigma\,,$$
$$\overline{\overline{p}}_t(s) = \frac{1}{2\pi R}\int_{\partial\Sigma(s)} p_t\, d\Sigma\,,$$

where $\boldsymbol{n}$ is the normal vector to the cross section $\Sigma(s)$ and $d\Sigma = r d\theta dr$ is an infinitesimal element of $\Sigma(s)$ and finally $\overline{\overline{p}}_t$ is the mean interstitial pressure on the boundary of a section Σ. The function $\phi(r,\theta)$ is a shape factor that is represented as

$$\Phi(r,\theta) = \phi(r/R)(1 + ar\cos\theta + br\sin\theta + cr^2\cos\theta\sin\theta + dr^2\cos^2\theta + er^2\sin^2\theta)\,, \quad (17.20)$$

where $a,\ b,\ c,\ d,\ e$ are parameters to be determined in what follows. The radially symmetric part of the profile, namely $\phi(r/R)$ is usually modeled as,

$$\phi(\rho) = \frac{\gamma+2}{\gamma}(1-\rho^\gamma)\,,$$

which coincides with the classic Poiseuille parabolic flow profile (observed in straight cylindrical channels) for $\gamma = 2$.

We aim to find a suitable expression for the parameters a, b, c, d, e in terms of the geometry of the centerline, namely $\mathbf{\Psi}$, such that the shape factor coincides with the classic parabolic Poiseuille profile when the centerline is rectilinear, while it deviates from this pattern when the centerline is curved. To this purpose, we set the following additional assumptions: **choice of** θ - we assume that on each cross section the axis $\theta = 0$ is colinear with the vector $\mathbf{N}$; **symmetry of the profile** - we require that the velocity profile in each section is such that $\Phi(r,\theta,\psi) = \Phi(r,-\theta,\psi) \quad \forall r,\theta,\psi$. As a result of that the coefficient b, c must vanish, namely $b = c = 0$; **linear dependence** - we assume that the correction factor of the velocity profile at any point s, namely $(1 + ar\cos\theta + br\sin\theta + cr^2\cos\theta\sin\theta + dr^2\cos^2\theta + er^2\sin^2\theta)$ is linearly dependent of the distance from the center of the osculating circle relative to this point.

We are now able to determine the coefficients a, d, e which satisfy these assumptions. For the linear dependence of the velocity with the distance from the center of the osculating circle, our profile must be zero in $C_0 = (r = 1/\kappa, \theta = 0, \psi)$, that is $(1 + a/\kappa + d/\kappa^2) = 0 \rightarrow d = -a\kappa - \kappa^2$. Furthermore, since the velocity profile is linearly dependent to the distance from the center of the osculating circle, we have that all the points with distance $1/\kappa$ from it must have the same velocity. The set of points of each cross section with distance $1/\kappa$ from the point C_0 are:

$$\varphi = \{(r, \theta) : \quad r = \frac{2\cos\theta}{\kappa}, \quad \theta \in [-\frac{\pi}{2}; +\frac{\pi}{2}]\}.$$

Moreover we have that $\Phi(r = 0, \theta, \psi) = \phi(0)$ and so $\forall (r, \theta) \in \phi$ then $\Phi(r, \theta, \psi) = \phi(r/R)$. It follows that $\forall (r, \theta) \in \varphi$:

$$0 = ar\cos\theta + dr^2\cos^2\theta + er^2\sin^2\theta = 2\frac{a}{\kappa}\cos^2\theta + 4\frac{d}{\kappa^2}\cos^4\theta + 4\frac{e}{\kappa^2}\cos^2\theta\sin^2\theta.$$

Now for $\theta = \pm\frac{\pi}{2}$ the equation is verified. In the other cases we can divide all by $2\cos^2\theta/\kappa^2$, to obtain:

$$0 = a\kappa + 2d\cos^2\theta + 2e\sin^2\theta \qquad \forall\theta \in \left(-\frac{\pi}{2}, +\frac{\pi}{2}\right).$$

To find the value of the parameters we need two more equations. Thus, we test it on two particular cases: $\theta = \pi/4, \theta = \pi/3$. For $\theta = \pi/4$, using $d = -a\kappa - \kappa^2$ we obtain:

$$0 = a\kappa + 2d(\frac{1}{2}) + 2e(\frac{1}{2}) = a\kappa + d + e = a\kappa - \kappa^2 - a\kappa + e = e - \kappa^2.$$

For that $e = \kappa^2$. Finally for $\theta = \pi/3$, using the previous result we have:

$$0 = a\kappa + 2d(\frac{1}{4}) + 2e(\frac{3}{4}) = a\kappa + \frac{d}{2} + \frac{3e}{2} = a\kappa - \frac{\kappa^2}{2} - \frac{a\kappa}{2} + \frac{3\kappa^2}{2} = \frac{a\kappa}{2} + \kappa^2$$

So we obtain $a = -2\kappa$ and $d = \kappa^2$. In a general configuration the curvature is dependent on the arc length $\kappa = \kappa(s)$. In conclusion, the velocity profile is of the form:

$$\Phi(r, \theta, \psi) = \phi(rR^{-1})(1 + r^2\kappa^2(\psi) - 2\kappa(\psi)r\cos\theta). \tag{17.21}$$

A visualization of such profile is provided in Figure 17.3

Now we derive the reduced model for flow in curved vessels by replacing the velocity profile (17.21) into the mass and momentum balance equations (17.19) and we integrate these equations on a portion of vessel, P delimited by two cross sections $\Sigma(s_1), \Sigma(s_2),\ s_2 > s_1$. In this way, we obtain simplified equations that

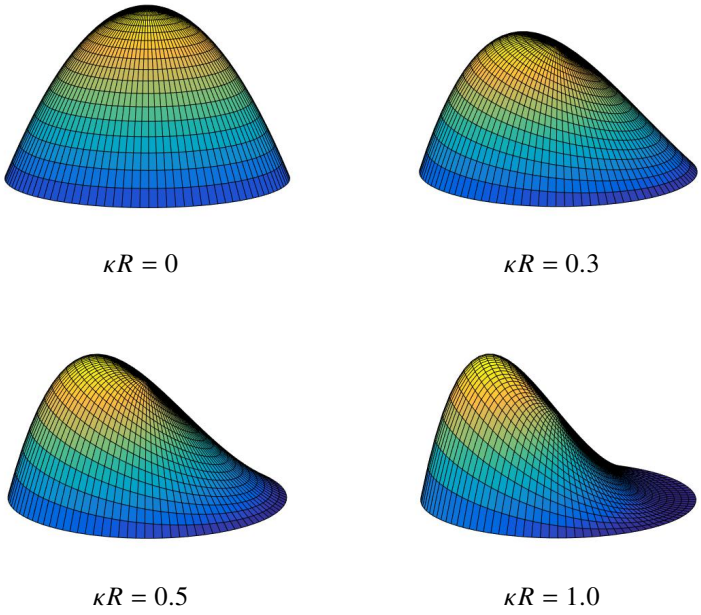

FIGURE 17.3 Velocity profiles in a curved, cylindrical pipe. Visualization of the dimensionless velocity profile for a curved pipe obtained using expression (17.21). In all cases, The shape parameter is $\gamma = 2$.

depend only on the arc length s. We start first from the continuity equation, using the fact that $\boldsymbol{n} = \boldsymbol{e}_s$ on $\Sigma(s_1)$ and $\Sigma(s_2)$ we obtain:

$$\begin{aligned}
0 = \int_P \nabla \cdot \boldsymbol{u}_v d\Omega &= \int_{\partial P} \boldsymbol{u}_v \cdot \mathbf{n}\, d\Sigma \\
&= \int_{\Sigma(s_1)} \boldsymbol{u}_v \cdot \boldsymbol{n} d\Sigma + \int_{\Sigma(s_2)} \boldsymbol{u}_v \cdot \boldsymbol{n}\, d\Sigma + \int_\Gamma \boldsymbol{u}_v \cdot \boldsymbol{n}\, d\Sigma \\
&= -\int_{\Sigma(s_1)} u_v\, d\Sigma + \int_{\Sigma(s_2)} u_v\, d\Sigma + \int_\Gamma f(p_t, p_v)\, d\Sigma \\
&\simeq -\overline{u}_v(s_1)\pi R^2(s_1) + \overline{u}_v(s_2)\pi R^2(s_2) + \int_{s_1}^{s_2} f(\overline{p}_t, p_v) dz \\
&= \int_{s_1}^{s_2} [f(\overline{\overline{p}}_t, \overline{p}_v) + \partial_s(\pi R^2 \overline{u}_v)] dz\,. \qquad (17.22)
\end{aligned}$$

According to (17.19), in particular $\partial_r p_v = \partial_\theta p_v = 0$, we notice that $p_v(r, s, \theta) = \overline{p}_v(s)$. Furthermore, in equation (17.22) we have adopted the assumption that the radius of the capillary is small if compared to the domain Ω. More precisely, we have set that

$$\begin{aligned}
\int_\Gamma f(p_t, p_v)\, d\Sigma &= \int_{s_1}^{s_2} \int_0^{2\pi} f(p_t, p_v) R(s) d\theta\, ds \\
&= \int_{s_1}^{s_2} \int_0^{2\pi} f(p_t, \overline{p}_v) R(s) d\theta\, ds = \int_{s_1}^{s_2} 2\pi R(s) f(\overline{\overline{p}}_t, \overline{p}_v)\, ds\,,
\end{aligned}$$

where the last step holds true because $f(p_t, p_v)$ is a linear function of its arguments.

Let us now apply the averaging technique to the momentum balance equation, that is the last of (17.19). We have:

$$\begin{aligned}
&\int_P \Delta u_v\, d\Omega = \int_{\partial P} \nabla u_v \cdot \boldsymbol{n}\, d\Sigma \\
&= -\int_{\Sigma(s_1)} \partial_s u_v\, d\Sigma + \int_{\Sigma(s_2)} \partial_s u_v\, d\Sigma + \int_\Gamma \nabla u_v \cdot \boldsymbol{n}\, d\Sigma = \int_\Gamma \nabla u_v \cdot \boldsymbol{e}_r\, d\Sigma \\
&= \int_\Gamma \partial_r u_v d\Sigma = \int_\Gamma \overline{u}_v(s) \partial_r \Phi(r, \theta) d\Sigma \\
&= \int_\Gamma \overline{u}_v(s) R^{-1} \phi'(rR^{-1})(1 - 2\kappa r \cos\theta + \kappa^2 r^2) + \phi(rR^{-1})(2\kappa^2 r - 2\kappa \cos\theta)\, d\Sigma \\
&= \int_{s_1}^{s_2} \int_0^{2\pi} \overline{u}_v(s) \big(R^{-1}\phi'(1)(1 - \kappa\cos\theta + \kappa^2 R^2) + \phi(1)(2\kappa^2 R - 2\kappa\cos\theta)\big) R d\theta ds.
\end{aligned}$$

Now using the fact that $\phi(1) = 0$, the periodicity of $\cos\theta$, we obtain:

$$\int_P \Delta u_v\, d\Omega = \int_{s_1}^{s_2} 2\pi \phi'(1)(1 + \kappa^2 R^2) \overline{u}_v(s)\, ds,$$

such that the averaged/one-dimensional form of the momentum equation becomes

$$-2\pi\mu_v(s)\phi'(1)\big(1+\kappa^2(s)R^2\big)\overline{u}_v(s)+\pi R^2\partial_s\overline{p}_v(s)=0. \tag{17.23}$$

17.3.2 More complex geometries, vascular networks

Now that we have derived the 1D model equations we need to generalize them to a more complex topology. To this purpose, we decompose the network into branches, Λ_i, $i=1,...,N$. The branches are parametrized by the arc length s_i; a tangent unit vector $\boldsymbol{\lambda}_i$ is also defined over each branch, accounting for an arbitrary branch orientation. Differentiation over the branches is defined using the tangent unit vector, namely $\partial_{s_i} := \boldsymbol{\lambda}_i \cdot \nabla$ on Λ_i, i.e. ∂_{s_i} represents the projection of ∇ along $\boldsymbol{\lambda}_i$. So far, the equations that govern the flow in each branch of the network are uncoupled. In order to make the flow problem fully coupled we need to enforce constraints at the junctions of the branches. Junctions are defined as the points $\boldsymbol{y}$ such that

$$\boldsymbol{y}_j = \boldsymbol{\Psi}_i(s_i^*) = \boldsymbol{\Psi}_{\hat{\imath}}(s_{\hat{\imath}}^*),\ s_i^* \in \{0, L_i\}\ \forall i, \hat{\imath} = 1,\dots,N$$

Let us count the junctions with the index $j=1,2,\dots,M$ and let us denote with $\mathcal{K}_j$ the set of indices i such that $\boldsymbol{\Psi}_i(s_i^*)=\boldsymbol{y}_j$. These are the branches that join at the j-th junction. There may be branches that end inside or at the boundary of the domain Ω. The former are said *dead ends* and are denoted with $\boldsymbol{z}$. The indices of branches featuring a dead end are $i \in \mathcal{E}$. The latter points are called *boundary ends* and are identified by the symbol $\boldsymbol{x}$. The set of branches intersecting the outer boundary is $i \in \mathcal{B}$.

The branches that merge at the j-th junction can be subdivided according to different criteria. We present here two options, both useful later on. Let $\boldsymbol{\lambda}_i$ be the orientation of a given branch of the network and let $\boldsymbol{e}_s$ be the *outgoing* tangential unit vector at the each of the two endpoints of the branch, identified respectively by the arc length coordinates $s_i=0$ and $s_i=L$.

The *ingoing points* are identified by the following conditions: $\boldsymbol{\lambda}_i \cdot \boldsymbol{e}_s(s_i) < 0$ for $s_i=0$ and $s_i=L$. The *outgoing* points are obviously the ones such that $\boldsymbol{\lambda}_i \cdot \boldsymbol{e}_s(s_i) > 0$. The indices i that correspond to ingoing branches at the j-th junction are denoted with $\mathcal{K}_j^-$, while the indices of the outgoing branches at the junction are collected in $\mathcal{K}_j^+$.

If we add the orientation of the flow to this classification we obtain that the *inflow points* are identified by the following condition that involves the orientation of the flow: $\overline{u}_v(s_i)\boldsymbol{\lambda}_i \cdot \boldsymbol{e}_s(s_i) < 0$ for $s_i=0$ and $s_i=L$. The *outflow* points are obviously the ones such that $\overline{u}_v(s_i)\boldsymbol{\lambda}_i \cdot \boldsymbol{e}_s(s_i) > 0$. The corresponding indices are collected in the sets $\mathcal{K}_j^{in}$, $\mathcal{K}_j^{out}$, respectively. We classify similarly the boundary ends, subdividing the points $\boldsymbol{x}$ into ingoing or outgoing, namely $\boldsymbol{x}^-, \boldsymbol{x}^+$, or into inflow and outflow $\boldsymbol{x}^{in}, \boldsymbol{x}^{out}$. At these points, we set the vascular pressure equal to a prescribed value $\overline{p}_v(\boldsymbol{x}_i) = g_v(\boldsymbol{x}_i),\ i \in \mathcal{B}$.

We enforce balance of flow rates and continuity of pressure at each junction, namely, $\sum_{i\in\mathcal{K}_j} \pi R_k^2 \overline{u}_{v,i} = 0$, $j = 1, 2, \ldots, M$, $\overline{p}_{v,i} = \overline{p}_{v,\hat{\imath}}$, $i, \hat{\imath} \in \mathcal{K}_j$, $j = 1, 2, \ldots, M$. At dead ends of the network we set no-flow conditions $\pi R^2 \overline{u}_v|_{z_i} = 0$, $i \in \mathcal{E}$, where $|_{z_i}$ is a shorthand notation for the evaluation of a function (or better the whole term) in the point z_i.

In conclusion, the coupled model of blood flow in the network is the following,

$$\begin{cases} \partial_s\big(\pi R_i^2(s)\overline{u}_{v,i}(s)\big) & \\ \quad +2\pi R_i(s) f(\overline{\overline{p}}_t(s), \overline{p}_v(s)) = 0 & \text{on } \Lambda_i, \\ -2\pi\mu_{v,i}(s)\phi'(1)\big(1+\kappa_i^2(s)R_i^2(s)\big)\overline{u}_{v,i}(s) & \\ \quad +\pi R_i^2(s)\partial_s\overline{p}_{v,i}(s) = 0 & \text{on } \Lambda_i, \\ \sum_{i\in\mathcal{K}_j} \pi R_k^2 \overline{u}_{v,i}|_{\mathbf{y}_j} = 0 & j = 1, \ldots, M, \\ \overline{p}_{v,i}|_{\mathbf{y}_j} = \overline{p}_{v,\hat{\imath}}|_{\mathbf{y}_j} & i, \hat{\imath} \in \mathcal{K}_j, \\ \pi R^2 \overline{u}_v|_{z_i} = 0 & i \in \mathcal{E}, \\ \overline{p}_v|_{\mathbf{x}_i} = g_v & i \in \mathcal{B}. \end{cases} \tag{17.24}$$

where the index $i = 1, \ldots, N$ numbers the network branches and the index $j = 1, 2, \ldots, M$ numbers the network junctions. We notice that in the case of a straight, cylindrical, impermeable pipe, i.e. $\gamma = 2$, the coefficient $\phi'(1) = -4$ and $f(\overline{\overline{p}}_t, \overline{p}_v) = 0$, such that these equations coincide with the standard Poiseuille flow.

17.3.2.1 Weak formulation of the vascular network problem

Deriving the variational formulation for the whole network problem is not trivial in this case because the vessel variables $\overline{p}_v$ and $\overline{u}_v$ *may* be discontinuous at multiple junctions. For this reason, we derive a proper Green's formula for the network problem. First, we rewrite the integral over the whole network as a summation of the integrals over single branches, namely:

$$\sum_{i=1}^{N} \int_{\Lambda_i} \pi R_i^2 \, \frac{\partial \overline{p}_v}{\partial s} \, v_v \, ds = -\sum_{i=1}^{N} \int_{\Lambda_i} \pi R_i^2 \, \overline{p}_v \, \frac{\partial v_v}{\partial s} \, ds + \sum_{i=1}^{N} \pi R_i^2 \, [\, \overline{p}_v \, v_v \,]_{\Lambda_i^-}^{\Lambda_i^+}, \tag{17.25}$$

where Λ_i^- and Λ_i^+ represent the inflow and outflow boundaries of Λ_i, according to the orientation $\boldsymbol{\lambda}_i$. We reformulate the last term in the previous equation by isolating the terms relative to inflow junction nodes from those relative to

outflow nodes, namely

$$\sum_{i=1}^{N} \pi R_i^2 [\, \overline{p}_v \, v_v \,]_{\Lambda_i^-}^{\Lambda_i^+} = \sum_{j=1}^{M} \left[\sum_{i \in \mathcal{K}_j^{out}} \pi R_i^2 \, \overline{p}_v \, v_v \, |_{\mathbf{y}_j} - \sum_{i \in \mathcal{K}_j^{in}} \pi R_i^2 \, \overline{p}_v \, v_v \, |_{\mathbf{y}_j} \right] + \sum_{i \in \mathcal{B}} \pi R_i^2 \, \overline{p}_v \, v_v \, |_{\boldsymbol{x}_i} + \sum_{i \in \mathcal{E}} \pi R_i^2 \, \overline{p}_v \, v_v \, |_{\boldsymbol{z}_i}. \quad (17.26)$$

If the pressure is continuous at the junction, we finally factorize out the pressure and isolate a term that corresponds to the junction conditions for the velocity test functions, that is

$$\sum_{j=1}^{M} \overline{p}_v(s_j) \left[\sum_{i \in \mathcal{K}_j^{out}} \pi R_i^2 \, v_v \, |_{\mathbf{y}_j} - \sum_{i \in \mathcal{K}_j^{in}} \pi R_i^2 \, v_v \, |_{\mathbf{y}_j} \right]. \quad (17.27)$$

The fluid mass conservation at each node can be expressed as follows

$$\sum_{i \in \mathcal{K}_j^{out}} \pi R_i^2 \, \overline{u}_v \, |_{\mathbf{y}_j} - \sum_{i \in \mathcal{K}_j^{in}} \pi R_i^2 \, \overline{u}_v \, |_{\mathbf{y}_j} = 0, \quad \forall j = 1, \ldots, M, \quad (17.28)$$

Then, we weakly enforce mass conservation into the variational formulation by multiplying (17.28) by the pressure test functions q_v, which act as a Lagrange multiplier for this constraint, namely

$$\sum_{j=1}^{M} q_v(s_j) \left[\sum_{i \in \mathcal{K}_j^{out}} \pi R_i^2 \, \overline{u}_v \, |_{\mathbf{y}_j} - \sum_{i \in \mathcal{K}_j^{in}} \pi R_i^2 \, \overline{u}_v \, |_{\mathbf{y}_j} \right]. \quad (17.29)$$

Finally, according to the previous equations, the weak formulation of the

vascular problem reads

$$
\begin{aligned}
&\sum_{i=1}^{N} \int_{\Lambda_i} -2\pi\mu_{v,i}(s)\phi'(1)\left(1+\kappa_i^2(s)R_i^2(s)\right)\overline{u}_v\, v_v\, ds \\
&\quad - \sum_{i=1}^{N} \int_{\Lambda_i} \pi R_i^2 \overline{p}_v\, \frac{\partial v_v}{\partial s}\, ds + \sum_{i\in\mathcal{E}} \pi R_i^2\, \overline{p}_v\, v_v\,|_{z_i} \\
&\quad + \sum_{j=1}^{M} \overline{p}_v(s_j) \left[\sum_{i\,\in\,\mathcal{K}_j^{out}} \pi R_i^2 v_v\,|_{\mathbf{y}_j} - \sum_{i\,\in\,\mathcal{K}_j^{in}} \pi R_i^2 v_v\,|_{\mathbf{y}_j} \right] \\
&\quad = \sum_{i\in\mathcal{B}} \pi R_i^2\, g_v\, v_v\,|_{\boldsymbol{x}_i},
\end{aligned}
\tag{17.30}
$$

$$
\begin{aligned}
&\sum_{i=1}^{N} \int_{\Lambda_i} \frac{\partial \pi R^2 \overline{u}_v}{\partial s}\, q_v\, ds + \sum_{i=1}^{N} \int_{\Lambda_i} 2\pi R_i(s) f(\overline{\overline{p}}_t(s), \overline{p}_v(s))\, q_v\, ds \\
&- \quad \sum_{j=1}^{M} q_v(s_j) \left[\sum_{i\,\in\,\mathcal{K}_j^{out}} \pi R_i^2 \overline{u}_v\,|_{\mathbf{y}_j} - \sum_{i\,\in\,\mathcal{K}_j^{in}} \pi R_i^2 \overline{u}_v\,|_{\mathbf{y}_j} \right] \\
&\quad - \sum_{i\in\mathcal{E}} \pi R_i^2\, q_v\, \overline{u}_v\,|_{z_i} \;=\; 0.
\end{aligned}
\tag{17.31}
$$

17.3.3 The embedded coupling conditions

Here we explicitly derive the coupling of the previous 1D model with the 3D model for the tissue introduced at the beginning. We notice that form the mathematical standpoint this is not a trivial task because the restriction of 3D fields to 1D manifolds is not necessarily well defined. For this reason, it is more convenient to address the coupling between the 1D and the 3D problems at the level of the variational formulation, following the approach proposed in Laurino, F. and Zunino, P. (2019).

We start with the derivation of the weak form of (17.17). First, we multiply both sides of (17.17) for a test function $q_t \in H^1(\Omega)$, integrating by parts and

using b(17.17) and (17.18), we obtain:

$$\begin{aligned}\int_{\Omega_t} \left[\nabla \cdot \boldsymbol{u}_t + L_p^{LF} \frac{S}{V}(p_t - p_0)\right] q_t \, d\Omega \\ = \int_{\Omega_t} \left[\boldsymbol{u}_t \cdot \nabla q_t + L_p^{LF} \frac{S}{V}(p_t - p_0) q_t\right] d\Omega - \int_{\partial\Omega_t} \boldsymbol{u}_t \cdot \boldsymbol{n} q_t \, d\gamma \\ = \int_{\Omega_t} \left[\boldsymbol{u}_t \cdot \nabla q_t + L_p^{LF} \frac{S}{V}(p_t - p_0) q_t\right] d\Omega + \int_{\partial\Omega_t} \beta_t (p_t - p_0) q_t \, d\gamma \\ - \int_\Gamma f(p_t, p_v) q_t \, d\gamma \,. \quad (17.32)\end{aligned}$$

Now, we apply a topological model reduction of the interface conditions, namely we go from a 3D-3D to a 3D-1D formulation. To this purpose, let us write the solution and the test functions on every cross section $\partial\mathcal{D}(s)$ as their average plus some fluctuation (in space, just like in turbulence modeling),

$$p_t = \overline{\overline{p}}_t + \tilde{p}_t, \quad \text{on } \partial\mathcal{D}(s)\,,$$

where $\overline{\tilde{u}}_t = 0$. Therefore, using the coordinates system (r, s, t) on Γ, and reminding that $f(p_t, p_v)$ is a linear function of its arguments, we have,

$$\begin{aligned}\int_\Gamma f(p_t, p_v) q_t \, d\Sigma = \int_\Lambda \int_{\partial\mathcal{D}(s)} f(\overline{\overline{p}}_t + \tilde{p}_t, \overline{\overline{p}}_v + \tilde{p}_v)(\overline{\overline{q}}_t + \tilde{q}_t) d\gamma ds \\ = \int_\Lambda |\partial\mathcal{D}(s)| f(\overline{\overline{p}}_t, \overline{\overline{p}}_v) \overline{\overline{q}}_t \, ds + \int_\Lambda \int_{\partial\mathcal{D}(s)} f(\tilde{p}_t, \tilde{p}_v) \tilde{q}_t \, d\gamma ds \,.\end{aligned}$$

Then, we make the following modelling assumptions: (i) we identify the domain Ω_t with the entire Ω, and we correspondingly omit the subscript t to the functions defined on Ω_t, namely

$$\int_{\Omega_t} q_t \, d\omega \simeq \int_\Omega q \, d\omega \,.$$

(ii) we assume that the product of fluctuations is small, namely

$$\int_{\partial\mathcal{D}(s)} \tilde{p}_t \tilde{q}_t d\gamma \simeq 0 \,.$$

(iii) we assume that the pressure in the vascular domain has a uniform profile on each cross section of the vessel. As a result we identify the mean values $\overline{\overline{p}}_v = \overline{p}_v$ and from now on we write $f(\overline{\overline{p}}_t, \overline{p}_v)$ in the coupling term.

By means of the previous deductions, putting together the terms of the weak form of (17.17), we obtain that $\boldsymbol{u}_t$, q_t solve the following problem,

$$\int_\Omega \boldsymbol{u}_t \cdot \boldsymbol{v}_t d\Omega + \frac{K}{\mu_t} \int_\Omega \nabla p_t \cdot \boldsymbol{v}_t d\Omega = 0, \quad (17.33)$$

$$\int_{\Omega_t} \left[\boldsymbol{u}_t \cdot \nabla q_t + L_p^{LF} \frac{S}{V}(p_t - p_0) q_t \right] d\Omega + \int_{\partial\Omega_t} \beta_t (p_t - p_0) q_t \, d\gamma - \sum_{i=1}^{N} \int_{\Lambda_i} 2pi R_i f(\overline{\overline{p}}_t, \overline{p}_v) \overline{\overline{q}}_v \, d\gamma = 0. \quad (17.34)$$

Combining (17.33)-(17.34) with (17.30)-(17.31) we obtain the following embedded 3D-1D coupled weak formulation,

$$\begin{cases} \sum_{i=1}^{N} \int_{\Lambda_i} -2\pi \mu_{v,i} \phi'(1) \left(1 + \kappa_i^2 R_i^2\right) \overline{u}_v \, v_v \, ds \\ \quad - \sum_{i=1}^{N} \int_{\Lambda_i} \pi R_i^2 \overline{p}_v \, \dfrac{\partial v_v}{\partial s} \, ds + \sum_{i \in \mathcal{E}} \pi R_i^2 \, \overline{p}_v \, v_v \, |_{z_i} \\ \quad + \sum_{j=1}^{M} \overline{p}_v \left[\sum_{i \in \mathcal{K}_j^{out}} \pi R_i^2 v_v \, |_{\boldsymbol{y}_j} - \sum_{i \in \mathcal{K}_j^{in}} \pi R_i^2 v_v \, |_{\boldsymbol{y}_j} \right] \\ \quad = \sum_{i \in \mathcal{B}} \pi R_i^2 \, g_v \, v_v \, |_{\boldsymbol{x}_i}, \\ \\ \sum_{i=1}^{N} \int_{\Lambda_i} \dfrac{\partial \pi R^2 \overline{u}_v}{\partial s} \, q_v \, ds + \sum_{i=1}^{N} \int_{\Lambda_i} 2\pi R_i(s) f(\overline{\overline{p}}_t, \overline{p}_v) \, q_v \, ds \\ \quad - \sum_{j=1}^{M} q_v \left[\sum_{i \in \mathcal{K}_j^{out}} \pi R_i^2 \overline{u}_v \, |_{\boldsymbol{y}_j} - \sum_{i \in \mathcal{K}_j^{in}} \pi R_i^2 \overline{u}_v \, |_{\boldsymbol{y}_j} \right] \\ \quad - \sum_{i \in \mathcal{E}} \pi R_i^2 \, q_v \, \overline{u}_v \, |_{z_i} \; = \; 0. \\ \\ \int_\Omega \boldsymbol{u}_t \cdot \boldsymbol{v}_t d\Omega + \frac{K}{\mu_t} \int_\Omega \nabla p_t \cdot \boldsymbol{v}_t d\Omega = 0, \\ \\ \int_{\Omega_t} \left[\boldsymbol{u}_t \cdot \nabla q_t + L_p^{LF} \frac{S}{V}(p_t - p_0) q_t \right] d\Omega + \int_{\partial\Omega_t} \beta_t (p_t - p_0) q_t \, d\gamma \\ \quad - \sum_{i=1}^{N} \int_{\Lambda_i} 2pi R_i^2 f(\overline{\overline{p}}_t, \overline{p}_v) \overline{\overline{q}}_v \, d\gamma = 0. \end{cases} \quad (17.35)$$

For clarity, we write the corresponding differential formulation, specifically to highlight the coupling w=between the vascular and the tissue compartments of the model. Let us first define Defining by δ_Λ as the distribution of Dirac masses along the manifold Λ. Then, we see that the coupling between the two models takes place at the level of the fluid mass conservation and it reads ad follows

$$\begin{aligned} \nabla \cdot \boldsymbol{u}_t + L_p^{LF} \frac{S}{V}(p_t - p_0) - 2\pi R f(\overline{\overline{p}}_t, \overline{p}_v) \delta_\Lambda = 0, \quad \text{in } \Omega \\ \partial_s \left(\pi R^2 \overline{u}_v \right) + 2\pi R f(\overline{\overline{p}}_t, \overline{p}_v) = 0, \quad \text{on } \Lambda. \end{aligned} \quad (17.36)$$

17.3.4 A 3D-1D embedded model for mass transport

In this section we extend the model to the description of a passive scalar, transported by the blood stream. Such model is adequate for a fairly small chemical

specie, diluted into the plasma. We describe how such molecule diffuses within the interstitial space, it is transported by the movement of the interstitial fluid, and it is depleted by the cells. These well-known phenomena can be described by using the general framework of diffusion-advection-reaction equations.

The mass transport model is composed by 3D advection-diffusion-reaction equations defined in the two domains Ω_v and Ω_t. Consistently with the previous models, we can transform such equations into a 3D-1D geometrically embedded multiscale model for mass transport defined on Λ and Ω. For simplicity, we avoid the full derivation of such model and we present directly the strong form of the 3D-1D problem for mass transport. It is composed by the following equations governing the concentration of the transported molecule (denoted by C, representing its mass per unit volume):

$$\begin{cases} \nabla \cdot (-D_t \nabla C_t + \mathbf{u}_t \, C_t) + V_{max} \, C_t = J_C \, \delta_\Lambda \quad \text{on } \Omega \\ \pi R^2 \frac{\partial}{\partial s} \left(-D_v \frac{\partial C_v}{\partial s} + u_v \, C_v \right) = -J_C \quad \text{on } \Lambda \\ J_C = 2\pi R \, P^C (C_v - \overline{\overline{C}}_t) \\ \qquad +(1-\sigma^C) \left(\frac{C_v + \overline{\overline{C}}_t}{2} \right) f(\overline{\overline{p}}_t(s), \overline{p}_v(s)) \quad \text{on } \Lambda \\ C_v = C_{in}|_{\mathbf{x}_i} \quad i \in \mathcal{B}^{in} \\ -D_v \frac{\partial C_v}{\partial s}|_{\mathbf{x}_i} \quad i \in \mathcal{B}^{out} \\ -D_t \nabla C_t \cdot \mathbf{n} = \beta_t^C \, (C_t - C_{0,t}) \quad \text{on } \partial\Omega \end{cases} \tag{17.37}$$

In the model (17.37), we specify the oxygen concentration at the vascular inlets and a null diffusive flux is imposed at the vascular outlets. For the tissue, we simulate the presence of an adjacent tissue domain with a boundary conductivity β_t^C and a far-field concentration C_0.

For the weak formulation of the model, necessary to enforce the mass balance conditions at the junctions of the network. To accomplish this, let us integrate the oxygen transport problem over Ω_v and multiply it by a smooth test function, q_v. We remark that the integration over the network Λ should be split into the integrals on each branch, denoted with Λ_i with $i = 0, \ldots, N$. Then, we integrate by parts the diffusion term on each branch to distribute the second derivative of C_v on the test function. Through these steps, the diffusion term is transformed

as follows:

$$-\int_\Lambda \pi R^2 D_v \frac{\partial^2 C_v}{\partial s^2}\varphi_v \, d\Lambda = -\sum_{i=0}^{N}\int_{\Lambda_i} \pi R_i^2 D_v \frac{\partial^2 C_v}{\partial s^2}\varphi_v \, d\Lambda_i$$
$$= \int_\Lambda \pi R^2 D_v \frac{\partial C_v}{\partial s}\frac{\partial \varphi_v}{\partial s} \, d\Lambda - \sum_{i=0}^{N} \pi R_i^2 \left[D_v \frac{\partial C_v}{\partial s}\varphi_v \right]_{\Lambda_i^-}^{\Lambda_i^+}. \quad (17.38)$$

Let Φ be the total mass flow rate along a capillary, expressed by the sum of convective mass flow rate and diffusive mass flow rate. Let us consider a junction of three micro-vessels (bifurcation or anastomosis) numbered as $i = 0, 1, 2$ where the index 0 represents the parent vessel and $1, 2$ are the daughter vessels. Mass conservation at junctions can be expressed as,

$$\Phi_0 = \Phi_1 + \Phi_2, \quad \Phi_i = \pi R_i^2 u_{v,i} C_{v,i} - \pi R_i^2 D_{v,i} \frac{\partial C_{v,i}}{\partial s}, \; i = 0, 1, 2. \quad (17.39)$$

We assume that the free oxygen concentration is continuous at the junction, but the velocities which may exhibit a jump at the junction points. As a result, the enforcement of (17.39) into (17.37) is not a trivial task. It is achieved by combining (17.39) with the fluid mass balance (17.24):

$$\pi R_0^2 u_{v_0} C_{v_0} = \pi R_1^2 u_{v_1} C_{v_1} + \pi R_2^2 u_{v_2} C_{v_2} \, . \quad (17.40)$$

Then, replacing (17.40) into (17.39), we obtain that the diffusive fluxes satisfy an independent balance law:

$$-D_v \frac{\partial C_{v_0}}{\partial s} = -D_v \frac{\partial C_{v_1}}{\partial s} - D_v \frac{\partial C_{v_2}}{\partial s} \, . \quad (17.41)$$

Going back to the variational formulation of mass transport in the vascular network (17.38), for a bifurcation or anastomosis (where the summation from $i = 0$ to $i = N = 2$ spans over the parent and daughter branches) we see that (17.41) can now be easily enforced as follows,

$$\sum_{i=0}^{N} \pi R_i^2 \left[D_v \frac{\partial C_v}{\partial s}\varphi_v \right]_{\Lambda_i^-}^{\Lambda_i^+} = \sum_{i=0}^{N} \pi R_i^2 \left[D_v \frac{\partial C_v}{\partial s} \right]_{\Lambda_i^-}^{\Lambda_i^+} \varphi_v = \sum_{i \in \mathcal{B}} \pi R_i^2 D_v \frac{\partial C_v}{\partial s} \, \varphi_v \Big|_{\boldsymbol{x}_i} .$$

Owing to the boundary conditions for C_v of system (17.37), the last term of the previous equation vanishes, because $\frac{\partial C_v}{\partial s}|_{\boldsymbol{x}_i} = 0$ for $i \in \mathcal{B}^{out}$ and $\varphi_v|_{\boldsymbol{x}_i} = 0$ for $i \in \mathcal{B}^{in}$, as Dirichlet boundary conditions are enforced at the inflow. As a result, the governing equation for free oxygen in the vascular bed, including mass conservation at the junctions, becomes,

$$\int_\Lambda \pi R^2 D_v \frac{\partial C_v}{\partial s}\frac{\partial \varphi_v}{\partial s} \, d\Lambda + \int_\Lambda \pi R^2 u_v \, C_v \varphi_v \, d\Lambda$$
$$+ \int_\Lambda \left[2\pi R \, P^C (C_v - \overline{\overline{C}}_t) + \frac{(1-\sigma^C)}{2} \, \phi_v \left(C_v + \overline{\overline{C}}_t \right) \right] \varphi_v \, d\Lambda = 0 \, . \quad (17.42)$$

We proceed similarly for the tissue equation, moving along the steps described before. We denote by φ_t the test function on the domain Ω. Therefore, the whole weak formulation of the oxygen transport problem results to be:

$$\begin{cases} \int_\Omega \left[D_t \nabla C_t \cdot \nabla \varphi_t + \nabla \cdot \mathbf{u}_t C_t \, \varphi_t + V_{max} C_t \varphi_t \right] d\Omega + \int_{\partial\Omega} \beta_t^C C_t \varphi_t d\gamma \\ \quad - \int_\Lambda \left[2\pi R \, P^C (C_v - \overline{\overline{C}}_t) + \frac{(1-\sigma^C)}{2} \, \phi_V \, \left(C_v + \overline{\overline{C}}_t \right) \right] \overline{\overline{\varphi}}_t ds \\ \quad = \int_{\partial\Omega} \beta_t^C C_{0,t} \varphi_t) d\gamma \,, \\ \\ \int_\Lambda \left[\pi R^2 D_v \, \frac{\partial C_v}{\partial s} \frac{\partial \varphi_v}{\partial s} + \pi R^2 u_v \, C_v \varphi_v \right] ds \\ \quad + \int_\Lambda \left[2\pi R \, P^C (C_v - \overline{\overline{C}}_t) + \frac{(1-\sigma^C)}{2} \, \phi_V \left(C_v + \overline{\overline{C}}_t \right) \right] \varphi_v ds = 0 \,. \end{cases} \tag{17.43}$$

17.3.5 Numerical simulations of oxygen transport

In this section we finally apply the mass transport model presented above to describe oxygen transfer in the vascular micro-environment. To this purpose some new features have to be added to the generic model for the transport of passive scalars. In particular, the oxygen transport model in the micro-vascular bed involves the red blood cells, namely the oxygen is transported in two different phases, free, C_v, and hemoglobin-bound, C_{HbO_2}, whose sum is the total oxygen in the microvasculature, called C_{tot}. The free oxygen diffuses through the capillary membrane and it is transported by the blood flow. In the blood, the oxygen flows both free and hemoglobin-bound, so it necessary to consider the total oxygen as sum of two contributes. For the interaction of oxygen with the erythrocytes into the bloodstream we consider the Hill curve that provides the hemoglobin saturation in terms of the partial pressure of dissolved oxygen. We remand the interested reader to Possenti et al. (2021) for all the details about this mesoscale computational model for microvascular oxygen transfer.

We present here some results that illustrate the behavior of the model in simple cases. We start with two simple geometrical settings, the bifurcation and the anastomosis, reported in Figure 17.4 respectively.

The radius of main branch is 4 μm while the one of the daughter branches is 3.17 μm according to Murray's law. However, in this particular case, the upper radius is increased of 10% while the lower one is decreased by 10%. This discrepancy generates the observable differences in the concentration profiles.

The velocity is a continuous quantity along the branch, but it assumes different values from branch to another, due to the effect of changing radius. The +10% variation of the radius significantly affects the distribution of flow rate downstream to the bifurcation, because resistance to flow is highly sensitive to the channel diameter of the channel. For what concerns the oxygen transport simulations we see that the free oxygen concentration is a continuous quantity. As a consequence of this, the mass balance is maintained. The C_v changes in a

non-linear way with respect progressing along the bifurcation, as shown by the charts in Figure Figure 17.4 (top right panel). The 10% variation of the radii brings an evident variation at the downstream of the bifurcation. Taking into account the lower branch, the oxygen tends to diffuse more easily due to the reduction of blood velocity.

For the oxygen dynamics in the anastomosis, see Figure 17.4 (bottom panel), we observe that near the junction the concentration in the lower branch features a U-shaped profile. This effect can be interpreted observing that the inlet branches feature different blood velocities. Then, the free oxygen concentration exchanges a different amount of oxygen with the interstitium. Near the junction, the curves join together due to a concentration balance condition. Overall, these results show qualitatively that the mass balance conditions are respected at the junction point and the dissolved oxygen concentration exhibits a physically reasonable behavior.

We finally show the output of the whole microvascular model (including blood flow, hematocrit transport and oxygen delivery, as described in Possenti et al. (2021)). The results of the simulations performed on a small portion of a realistic vascular network are reported in Figure 17.5. These results illustrate the potential of the 3D-1D embedded coupling approach to describe the miscrovascular environment. The reader interested to these topics is referred to Cattaneo and Zunino (2014a,b); Nabil et al. (2015); Nabil and Zunino (2016) for applications to cancer, to Possenti et al. (2020) for applications to edema, to Possenti et al. (2021) for applications to radiotherapy.

17.4 CONCLUSIONS

In this chapter we have reviewed some recent developments about modeling the cardiovascular system. In particular we have described those models that are based on coupled partial differential equations on domains of different dimensionality. Starting from the seminal works on the *sequential* coupling of 3D with 1D models, we have shown that the *embedded* coupling is also possible and interesting in different scenarios. In conclusion, we believe that the *geometric multiscale* approaches for modeling the cardiovascular system are still a vivid area of research the potential of which has not been fully exploited yet.

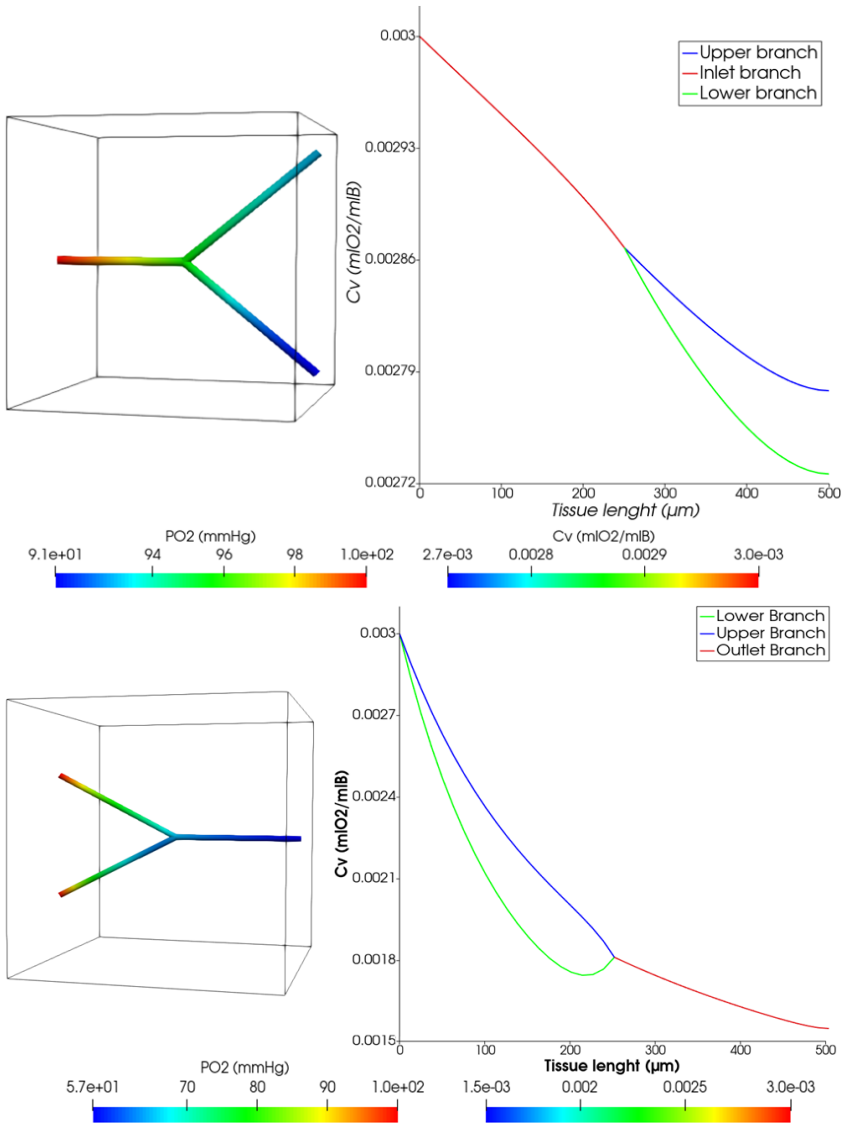

FIGURE 17.4 Oxygen transport in a bifurcation and anastomosis. The dissolved oxygen concentration C_v in a bifurcation (top panel) and an anastomosis (bottom panel). The inflow concentration (on the left side) is fixed to the level of normally oxygenated blood.

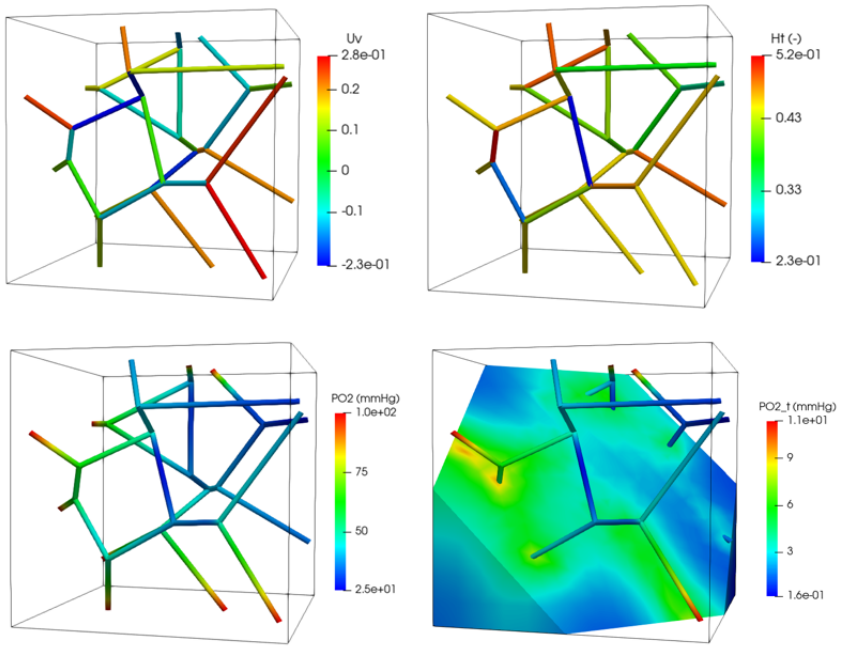

FIGURE 17.5 oxygen transfer in the microvascular environment. Simulation of the blood velocity in a vascular network (u_v, top left panel), the hematocrit transported by the blood (Ht top right panel), the dissolved oxygen in the vessels (quantified as oxygen partial pressure, p_{O_2}, bottom left panel) and the oxygen transferred to the tissue (quantified as oxygen partial pressure, bottom right panel).

References

J. Alastruey, K. H. Parker, J. Peiró, S. M. Byrd, and S. J. Sherwin. Modelling the circle of Willis to assess the effects of anatomical variations and occlusions on cerebral flows. *Journal of Biomechanics*, 40(8):1794–1805, Jan. 2007. ISSN 0021-9290. doi: 10.1016/j.jbiomech.2006.07.008.

J. Alastruey, S. M. Moore, K. H. Parker, T. David, J. Peiró, and S. J. Sherwin. Reduced modelling of blood flow in the cerebral circulation: Coupling 1-D, 0-D and cerebral auto-regulation models. *International Journal for Numerical Methods in Fluids*, 56(8):1061–1067, Mar. 2008. doi: 10.1002/fld.1606.

D. Ambrosi, A. Quarteroni, and G. Rozza, editors. *Modeling of Physiological Flows*, volume 5 of *Modeling, Simulation and Applications*. Springer-Verlag, 2012.

L. Bennati, C. Vergara, M. Domanin, C. Malloggi, D. Bissacco, S. Trimarchi, V. Silani, G. Parati, and R. Casana. A computational fluid–structure interaction study for carotids with different atherosclerotic plaques. *Journal of Biomechanical Engineering*, 143(9), May 2021. ISSN 0148-0731. doi: 10.1115/1.4050910.

S. Bertoluzza, A. Decoene, L. Lacouture, and S. Martin. Local error estimates of the finite element method for an elliptic problem with a Dirac source term. *Numerical Methods for Partial Differential Equations*, 34(1):97–120, 2018.

T. R. Blake and J. F. Gross. Analysis of coupled intra- and extraluminal flows for single and multiple capillaries. *Mathematical Biosciences*, 59(2):173–206, 1982.

P. J. Blanco, S. M. Watanabe, M. A. R. F. Passos, P. A. Lemos, and R. A. Feijóo. An anatomically detailed arterial network model for one-dimensional computational hemodynamics. *IEEE transactions on bio-medical engineering*, 62(2):736–753, Feb. 2015. ISSN 1558-2531. doi: 10.1109/TBME.2014.2364522.

L. Cattaneo and P. Zunino. Computational models for fluid exchange between microcirculation and tissue interstitium. *Networks and Heterogeneous Media*, 9(1):135–159, 2014a. ISSN 1556-1801. doi: 10.3934/nhm.2014.9.135.

L. Cattaneo and P. Zunino. A computational model of drug delivery through microcirculation to compare different tumor treatments. *International Journal for Numerical Methods in Biomedical Engineering*, 30(11):1347–1371, 2014b. doi: 10.1002/cnm.2661.

P. Causin, J. Gerbeau, and F. Nobile. Added-mass effect in the design of partitioned algorithms for fluid–structure problems. *Computer Methods in Applied Mechanics and Engineering*, 194 (42-44):4506–4527, Oct. 2005. doi: 10.1016/j.cma.2004.12.005.

A. Cicchetti, F. Laurino, L. Possenti, T. Rancati, and P. Zunino. In silico model of the early effects of radiation therapy on the microcirculation and the surrounding tissues. *Physica Medica*, 73: 125–134, 2020. doi: 10.1016/j.ejmp.2020.04.006.

P. Crosetto, P. Reymond, S. Deparis, D. Kontaxakis, N. Stergiopulos, and A. Quarteroni. Fluid–structure interaction simulation of aortic blood flow. *Computers & Fluids*, 43(1):46–57, Apr. 2011. ISSN 0045-7930. doi: 10.1016/j.compfluid.2010.11.032.

C. D'Angelo. *Multi scale modelling of metabolism and transport phenomena in living tissues*. PhD thesis, EPFL, Lausanne, 2007.

C. D'Angelo. Finite element approximation of elliptic problems with Dirac measure terms in weighted spaces: Applications to one-and three-dimensional coupled problems. *SIAM Journal on Numerical Analysis*, 50(1):194–215, 2012.

C. D'Angelo and A. Quarteroni. On the coupling of 1D and 3D diffusion-reaction equations: Application to tissue perfusion problems. *Mathematical Models and Methods in Applied Sciences*,

18(08):1481–1504, 2008.

G. J. Fleischman, T. W. Secomb, and J. F. Gross. The interaction of extravascular pressure fields and fluid exchange in capillary networks. *Mathematical Biosciences*, 82(2):141–151, 1986.

G. J. Flieschman, T. W. Secomb, and J. F. Gross. Effect of extravascular pressure gradients on capillary fluid exchange. *Mathematical Biosciences*, 81(2):145–164, 1986.

L. Formaggia and C. Vergara. Prescription of general defective boundary conditions in fluid-dynamics. *Milan Journal of Mathematics*, 77(2010):333–350, Aug. 2012. ISSN 1424-9286. doi: 10.1007/s00032-012-0185-8.

L. Formaggia, F. Nobile, A. Quarteroni, and A. Veneziani. Multiscale modelling of the circulatory system: A preliminary analysis. *Computing and visualization in Science*, 83:75–83, 1999.

L. Formaggia, J. F. Gerbeau, F. Nobile, and A. Quarteroni. On the coupling of 3D and 1D Navier–Stokes equations for flow problems in compliant vessels. *Computer Methods in Applied Mechanics and Engineering*, 191(6-7):561–582, 2001. doi: 10.1016/S0045-7825(01)00302-4.

L. Formaggia, D. Lamponi, M. Tuveri, and A. Veneziani. Numerical modeling of 1D arterial networks coupled with a lumped parameters description of the heart. *Computer Methods in Biomechanics and Biomedical Engineering*, 9(5):273–288, 2006. doi: 10.1080/10255840600857767.

L. Formaggia, A. Quarteroni, and A. Veneziani. *Cardiovascular Mathematics: Modeling and Simulation of the Circulatory System*, volume 1. Springer Science & Business Media, 2010a.

L. Formaggia, A. Veneziani, and C. Vergara. Flow rate boundary problems for an incompressible fluid in deformable domains: Formulations and solution methods. *Computer Methods in Applied Mechanics and Engineering*, 199(9-12):677–688, Jan. 2010b. doi: 10.1016/j.cma.2009.10.017.

L. Formaggia, A. Quarteroni, and C. Vergara. On the physical consistency between three-dimensional and one-dimensional models in haemodynamics. *Journal of Computational Physics*, 244 (227058):97–112, 2012. doi: 10.1016/j.jcp.2012.08.001.

L. Formaggia, A. Fumagalli, A. Scotti, and P. Ruffo. A reduced model for Darcy's problem in networks of fractures. *ESAIM: Mathematical Modelling and Numerical Analysis*, 48(4):1089–1116, 2014.

I. G. Gjerde, K. Kumar, and J. M. Nordbotten. A singularity removal method for coupled 1D–3D flow models. *Computational Geosciences*, pages 1–15, 2019.

A. C. Guyton, H. J. Granger, and A. E. Taylor. Interstitial fluid pressure. *Physiological reviews*, 51 (3):527–63, 1971. ISSN 0031-9333.

G. Hartung, S. Badr, M. Moeini, F. Lesage, D. Kleinfeld, A. Alaraj, and A. Linninger. Voxelized simulation of cerebral oxygen perfusion elucidates hypoxia in aged mouse cortex. *PLoS Computational Biology*, 17(1), 2021. doi: 10.1371/JOURNAL.PCBI.1008584.

T. Koch, K. Heck, N. Schröder, H. Class, and R. Helmig. A new simulation framework for soil–root interaction, evaporation, root growth, and solute transport. *Vadose Zone Journal*, 17(1), 2018.

T. Köppl and B. Wohlmuth. Optimal a priori error estimates for an elliptic problem with Dirac right-hand side. *SIAM Journal on Numerical Analysis*, 52(4):1753–1769, 2014.

T. Köppl, E. Vidotto, and B. Wohlmuth. A local error estimate for the Poisson equation with a line source term. In *Numerical Mathematics and Advanced Applications ENUMATH 2015*, pages 421–429. Springer, 2016.

M. Kuchta, M. Nordaas, J. Verschaeve, M. Mortensen, and K. Mardal. Preconditioners for saddle point systems with trace constraints coupling 2d and 1d domains. *SIAM Journal on Scientific Computing*, 38(6):B962–B987, 2016.

M. Kuchta, K.-A. Mardal, and M. Mortensen. Preconditioning trace coupled 3d-1d systems using fractional Laplacian. *Numerical Methods for Partial Differential Equations*, 35(1):375–393, 2019. doi: https://doi.org/10.1002/num.22304. URL `https://onlinelibrary.wiley.com/doi/abs/10.1002/num.22304`.

M. Kuchta, F. Laurino, K.-A. Mardal, and P. Zunino. Analysis and approximation of mixed-dimensional PDEs on 3D-1D domains coupled with Lagrange multipliers. *SIAM Journal on Numerical Analysis*, 59(1):558–582, 2021. doi: 10.1137/20M1329664.

D. Kumar, R. Vinoth, A. Raviraj, and C. S. Vijay Shankar. Non-Newtonian and Newtonian blood flow in human aorta: A transient analysis. *Biomedical Research*, 28(7):3194–3203, Jan. 2017. ISSN 0970-938X.

T. Köppl, E. Vidotto, B. Wohlmuth, and P. Zunino. Mathematical modeling, analysis and numerical approximation of second-order elliptic problems with inclusions. *Mathematical Models and Methods in Applied Sciences*, 28(5):953–978, 2018. doi: 10.1142/S0218202518500252.

E. M. Landis and J. R. Pappenheimer. Exchange of substances through the capillary walls. In W. F. Hamilton, editor, *Handbook of Physiology. Circulation*, chapter 29, pages 961–1034. Am. Physiol. Soc., Washington, DC, 1963.

Laurino, F. and Zunino, P. Derivation and analysis of coupled PDEs on manifolds with high dimensionality gap arising from topological model reduction. *ESAIM: Mathematical Modelling and Numerical Analysis*, 53(6):2047–2080, 2019.

A. C. I. Malossi, P. J. Blanco, P. Crosetto, S. Deparis, and A. Quarteroni. Implicit coupling of one-dimensional and three-dimensional blood flow models with compliant vessels. *Multiscale Modeling & Simulation*, 11(2):474–506, Jan. 2013. ISSN 1540-3459. doi: 10.1137/120867408.

V. Martin, F. Clément, A. Decoene, and J.-F. Gerbeau. Parameter identification for a one-dimensional blood flow model. *ESAIM: Proceedings*, 14:174–200, 2005. ISSN 1270-900X. doi: 10.1051/proc:2005014.

V. Milišić and A. Quarteroni. Analysis of lumped parameter models for blood flow simulations and their relation with 1D models. *ESAIM: Mathematical Modelling and Numerical Analysis*, 38(4): 613–632, July 2004. doi: 10.1051/m2an:2004036.

M. Nabil and P. Zunino. A computational study of cancer hyperthermia based on vascular magnetic nanoconstructs. *Royal Society Open Science*, 3(9), 2016. doi: 10.1098/rsos.160287.

M. Nabil, P. Decuzzi, and P. Zunino. Modelling mass and heat transfer in nano-based cancer hyperthermia. *Royal Society Open Science*, 2(10), 2015. doi: 10.1098/rsos.150447.

G. S. Offeddu, L. Possenti, J. T. Loessberg-Zahl, P. Zunino, J. Roberts, X. Han, D. Hickman, C. G. Knutson, and R. D. Kamm. Application of transmural flow across in vitro microvasculature enables direct sampling of interstitial therapeutic molecule distribution. *Small*, 15(46), 2019. doi: 10.1002/smll.201902393.

D. W. Peaceman. Interpretation of well-block pressures in numerical reservoir simulation. *Soc Pet Eng AIME J*, 18(3):183–194, 1978.

D. W. Peaceman. Interpretation of well-block pressures in numerical reservoir simulation with nonsquare grid blocks and anisotropic permeability. *Society of Petroleum Engineers journal*, 23 (3):531–543, 1983.

L. Possenti, G. Casagrande, S. Di Gregorio, P. Zunino, and M. L. Costantino. Numerical simulations of the microvascular fluid balance with a non-linear model of the lymphatic system. *Microvascular Research*, 122:101–110, 2019a.

L. Possenti, S. di Gregorio, F. M. Gerosa, G. Raimondi, G. Casagrande, M. L. Costantino, and P. Zunino. A computational model for microcirculation including Fahraeus-Lindqvist effect, plasma skimming and fluid exchange with the tissue interstitium. *International Journal for Numerical Methods in Biomedical Engineering*, 35(3), 2019b. doi: 10.1002/cnm.3165.

L. Possenti, S. Di Gregorio, G. Casagrande, M. L. Costantino, T. Rancati, and P. Zunino. A global sensitivity analysis approach applied to a multiscale model of microvascular flow. *Computer Methods in Biomechanics and Biomedical Engineering*, pages 1215–1224, 2020. doi: 10.1080/10255842.2020.1793964.

L. Possenti, A. Cicchetti, R. Rosati, D. Cerroni, M. L. Costantino, T. Rancati, and P. Zunino. A mesoscale computational model for microvascular oxygen transfer. *Annals of Biomedical Engineering*, June 2021. ISSN 1573-9686. doi: 10.1007/s10439-021-02807-x.

P. Reymond, Y. Bohraus, F. Perren, F. Lazeyras, and N. Stergiopulos. Validation of a patient-specific one-dimensional model of the systemic srterial tree. *American Journal of Physiology. Heart and Circulatory Physiology*, 301(3):H1173–1182, Sept. 2011. ISSN 1522-1539. doi: 10.1152/ajpheart.00821.2010.

R. Savabi, M. Nabaei, S. Farajollahi, and N. Fatouraee. Fluid structure interaction modeling of aortic arch and carotid bifurcation as the location of baroreceptors. *International Journal of Mechanical Sciences*, 165:105222, Jan. 2020. ISSN 0020-7403. doi: 10.1016/j.ijmecsci.2019.105222.

T. Secomb, R. Hsu, E. Park, and M. Dewhirst. Green's function methods for analysis of oxygen delivery to tissue by microvascular networks. *Annals of Biomedical Engineering*, 32(11):1519–1529, 2004.

M. A. Swartz and M. E. Fleury. Interstitial flow and its effects in soft tissues. *Annual Review of Biomedical Engineering*, 9(1):229–256, 2007. ISSN 1523-9829. doi: 10.1146/annurev.bioeng.9.060906.151850.

P. W. Sweeney, A. D'Esposito, S. Walker-Samuel, and R. J. Shipley. Modelling the transport of fluid through heterogeneous, whole tumours in silico. *PLoS Computational Biology*, 15(6), 2019. doi: 10.1371/journal.pcbi.1006751.

E. F. Toro and A. Siviglia. Flow in collapsible tubes with discontinuous mechanical properties: Mathematical model and exact solutions. *Communications in Computational Physics*, 13(2): 361–385, Feb. 2013. doi: 10.4208/cicp.210611.240212a.

A. Veneziani and C. Vergara. Flow rate defective boundary conditions in haemodynamics simulations. *International Journal for Numerical Methods in Fluids*, 47(8-9):803–816, 2005. ISSN 1097-0363. doi: 10.1002/fld.843.

MOX Technical Reports, last issues

Dipartimento di Matematica
Politecnico di Milano, Via Bonardi 9 - 20133 Milano (Italy)

98/2023 Lespagnol, F.; Grandmont, C.; Zunino, P.; Fernandez, M.A.
A mixed-dimensional formulation for the simulation of slender structures immersed in an incompressible flow

100/2023 Vitullo, P.; Cicci, L.; Possenti, L.; Coclite, A.; Costantino, M.L.; Zunino, P.
Sensitivity analysis of a multi-physics model for the vascular microenvironment

96/2023 Bonetti, S.; Botti, M.; Antonietti, P.F.
Robust discontinuous Galerkin-based scheme for the fully-coupled non-linear thermo-hydro-mechanical problem

95/2023 Barnafi, N. A.; Regazzoni, F.; Riccobelli, D.
Reconstructing relaxed configurations in elastic bodies: mathematical formulation and numerical methods for cardiac modeling

93/2023 Andrini, D.; Magri, M.; Ciarletta, P.
Optimal surface clothing with elastic nets

92/2023 Burzacchi, A.; Rossi, L.; Agasisti, T.; Paganoni, A. M.; Vantini, S.
Commuting time as a determinant of higher education students' performance: the case of Politecnico di Milano

Burzacchi, A.; Rossi, L.; Agasisti, T.; Paganoni, A. M.; Vantini, S.
Commuting time as a determinant of higher education students' performance: the case of Politecnico di Milano

90/2023 Gregorio, C.; Baj, G.; Barbati, G.; Ieva, F.
Dynamic treatment effect phenotyping through functional survival analysis

88/2023 Masci, C.; Spreafico, M.; Ieva, F.
Joint modelling of recurrent and terminal events with discretely-distributed non-parametric frailty: application on re-hospitalizations and death in heart failure patients

89/2023 Savaré, L.; Ieva, F.; Corrao, G.; Lora, A.
Capturing the variety of clinical pathways in patients with schizophrenic disorders through state sequences analysis